Detection of Temporal Change in Near-Source Attenuation Affected by Fluid Migration in the Source Region of Intense Earthquake Swarm in the Yamagata-Fukushima Border, NE Japan

Keisuke Yoshida[1*]

[1]Research Center for Prediction of Earthquakes and Volcanic Eruptions, Graduate School of Science, Tohoku University

Abbreviated Title: Temporal change in near-source attenuation

*Corresponding author: Tel: +81-22-795-6779; Fax: +81-22-264-3292; keisuke.yoshida.d7@tohoku.ac.jp; Address: 6-6 Aza-Aoba, Aramaki, Aoba-ku, Sendai, 980-8578, Japan

Summary

The behaviour of fluids in the crust is key to understanding earthquake occurrence due to the effect of fluid behaviour on fault strength. The attenuation of seismic waves may be locally high in fault zones as fluids are intensely distributed in these zones. This study uses a novel, simple approach to examine near-source attenuation in the focal region of intense swarm activity in the Yamagata-Fukushima border region, Japan. Near-source attenuation was estimated by determining the decay of amplitude ratios of nearby earthquake pairs with travel time differences precisely quantified using a waveform correlation. In the initial ~50 d, $\boldsymbol{Q^{-1}}$ was high, then it significantly decreased to become almost constant for the subsequent period. This pattern is similar to those independently observed for background seismicity rate, b-value, stress drop, and fault strength. These patterns can be attributed to the hypothesis that the swarm was triggered by fluid movement following the 2011 Tohoku-Oki earthquake, and the source and seismicity characteristics and the seismic attenuation were altogether affected by the temporal change in pore pressure. The method demonstrated in this study may be a useful tool to detect high pore pressure anomaly at depth and understand its relationship with earthquake occurrence.

Keywords: Seismic attenuation; Seismicity and tectonics; Earthquake source observations; Rheology and friction of fault zones; Elasticity and anelasticity

1 Introduction

The occurrence of earthquakes may be heavily influenced by increases in pore pressure as it decreases fault strength (Hasegawa et al., 2005; Hubbert & Rubey, 1959; Nur & Booker, 1972; Sibson, 1992). It is possible that the seismogenic zone has a larger amount of fluids than the surrounding crust (Mindaleva et al., 2020); as such, it is crucial to develop a means of monitoring the behaviour of fluid at depth to understand the mechanisms influencing earthquake occurrence.

The attenuation of seismic waves may be locally high in fault zones as fluids are intensely distributed in these zones (Winkler & Nur, 1982).The spatiotemporal variation of the seismic attenuation structure provides insight into the states of crust including the presence of fluids and fault damage (Hauksson & Shearer, 2006; Matsumoto et al., 2009; Nakajima & Matsuzawa, 2017). Previous studies have investigated the attenuation structure at the regional scale in many global locations, as summarised by Sato et al. (2012). However, few studies (Matsumoto et al., 2009; Wcislo et al., 2018; Kriegerowski et al., 2019) have attempted to directly estimate the attenuation structure near the earthquake source (hereafter referred as “near-source attenuation”). Near-source attenuation provides important information on the role of fluid in earthquake occurrence, and understanding near-source attenuation is also critical to accurately interpreting the source, path, and site-effects of seismic waveform data.

Few studies have attempted to estimate near-source attenuation using seismic waveforms of multiple, nearby earthquakes. Matsumoto et al. (2009) proposed a method to directly estimate the attenuation structure in a seismically active region based on multiple spectral ratios of two earthquakes. They used coda waves to remove the source-effects, computed spectral ratios at many different stations, and estimated the spatial variation of attenuation structure in the aftershock area of the 2005 M7.0 West Off Fukuoka Prefecture earthquake. They did not assume a specific frequency dependence of seismic attenuation or apparent source spectra. Kriegerowski et al. (2019) developed another method based on the spectral ratios of two earthquakes assuming that the attenuation structure was constant over the analysed frequency range and the source spectra completely followed the ω^2-model (Aki, 1967) at each station. Similarly, Wcisło et al. (2018) used differences in the peak frequency of event-pairs to estimate near-source attenuation for swarm activity in West Bohemia, in the Czech Republic. They also assumed that the attenuation factor was constant over frequency. Unlike Matsumoto et al. (2009), the methods used in Kriegerowski et al. (2019) and Wcisło et al. (2018) may provide an estimate of the attenuation structure, even from a single seismic station due to these additional assumptions. However, many of the results from Kriegerowski et al. (2019) possess unphysical negative values for the attenuation factor, which may be attributed to the errors of these assumptions. Previous studies have shown that the attenuation factor decreases with frequency greater than ~1 Hz, as summarised by Sato et al. (2012). This study develops a simple method with fewer assumptions than previous research, to estimate near-source attenuation.

This study adopted a straightforward means of directly estimating near-source attenuation by determining the decay of amplitude ratios for two nearby earthquakes with travel time differences (Fig. 1). Typically, this analysis is not easy as it requires precise measurements of the arrival time difference and amplitude ratio from various seismic stations. To address this issues, this study uses the waveform correlation technique (Poupinet et al., 1984) to accurately quantify the differential arrival time and amplitude ratio.

This method was applied to the intense swarm activity in the crust of the Yamagata-Fukushima border region, Japan (Fig. 2a). Many earthquakes with similar focal mechanisms occurred within a small area of this source region (Yoshida et al., 2016, 2019a and 2019b; Yoshida & Hasegawa, 2018). They are characterised by WNW–ESE compressional reverse faulting, typical in NE Japan, especially before the 2011 Tohoku-Oki earthquake (Yoshida et al., 2012). Waveform similarities in the source region provides precise differential arrival time and amplitude ratio data using waveform cross-correlation (Yoshida & Hasegawa, 2018). The focal area is surrounded by the Japanese national dense seismic network, enabling the determination of near-source attenuation in the region.

Previous studies have suggested that the Yamagata-Fukushima border swarm was triggered by fluid movement, following the 2011 Tohoku-Oki earthquake (Terakawa et al., 2013; Yoshida et al., 2016, 2019a). Following a six day delay, the swarm activity began despite a reduction in shear stress after the 2011 Tohoku-Oki earthquake. Hypocentres illustrate distinct migration behaviour, similar to fluid-injection-induced seismicity (Shapiro et al., 1997), from deeper to shallow levels along several planar structures (Yoshida & Hasegawa, 2018). Previous studies have reported on temporal variations in hypocentres (Okada et al., 2015; Yoshida & Hasegawa, 2018), fault strength (Yoshida et al., 2016), stress drop (Yoshida et al., 2017, 2019b), b-values (Yoshida et al., 2017), and background seismicity rate (Yoshida & Hasegawa, 2018) in the source region of the swarm (Figs. 2b). These variations have been considered the outcomes of temporal changes in pore pressure. As such, it is of great interest to compare temporal changes in near-source attenuation with these source and seismicity parameters.

2 Theory, data, method and synthetic Test

2.1 Theory

The amplitude attenuation due to anelastic attenuation may be described by the seismic quality factor, $Q = -\frac{2\pi E}{\Delta E}$, where E is the energy of a seismic wave and ΔE is the energy lost during one cycle. In seismology, amplitude attenuation over elapsed time is related to Q^{-1} by the following approximation ($Q \gg 1$):

$$\ln\left(r^{\gamma} A\ (f)\right) = -\pi f Q^{-1}(f)t + C(f) \tag{1}$$

where f is frequency; $A(f)$ is the spectral amplitude; r is the distance from the source; γ is the exponent of the geometric spreading factor depending on the ray-path; t is the elapsed time; and $C(f)$ includes the source and site-effects on amplitude. Here, Q^{-1} is the combination of amplitude attenuations due to intrinsic absorption and scattering losses. In many regions of the world, the Q^{-1}above ~1 Hz ranges from 10^{-4} to 10^{-1}, and decreases with frequency (Sato et al., 2012).

This study uses the relationship between the amplitude ratios $A_{1\mathrm{i}}/A_{2\mathrm{i}}$ and the relative travel times, $\delta t_{\mathrm{i}} = t_{1\mathrm{i}} - t_{2\mathrm{i}}$, from two nearby (~1 km) earthquakes to estimate near-source attenuation (Fig. 1a). Here, $A_{1\mathrm{i}}$ and $A_{2\mathrm{i}}$ are the amplitudes, and $t_{1\mathrm{i}}$ and $t_{2\mathrm{i}}$ are the travel times for the two events (event-1 and event-2, respectively) at the i^{th} station. Assuming the same site and propagation effects along the shared pathway of the two nearby earthquakes:

$$\ln\frac{A_{1i}(f)}{A_{2i}(f)} = -\pi f Q^{-1}(f)\delta t_{\mathrm{i}} + \delta C_i(f) \tag{2}$$

here, $\delta C_i(f) = C_1(f) - C_2(f)$, where $C_1(f)$ and $C_2(f)$ correspond to $C(f)$ in Eq. (1) for event-1 and event-2 at the i^{th} station, respectively; and $\delta C_i(f)$ is the amplitude difference of source-effects of two earthquakes. The geometrical spreading effect was dismissed as the distance between the two earthquakes was much smaller (~1 km) than the distance between the earthquakes and the stations (>30 km).

To avoid the effects of the earthquake source process in Eq. (2), this study only uses data that satisfies two conditions; (1) the analysed frequency range needed to be sufficiently lower than the source corner frequencies, and (2) the focal mechanisms of the two earthquakes should be similar. As such, $\delta C_i(f)$ in Eq. (2) may be assumed as constant among stations, and $Q^{-1}(f)$ near the source can be estimated by precisely measuring the amplitude ratios $(A_{1\mathrm{i}}(f)/A_{2\mathrm{i}}(f))$ and the travel time differences (δt_{i}), at various stations. Note that even a frequency range higher than the corner frequency may be available if spectral falloffs were the same between two events (such as the ω-square model), and the corner frequencies were the same among different seismic stations for the earthquake pair. As such an assumption does not hold even for a simple physical source model (Kaneko & Shearer, 2014), this study only used a frequency range less than the source corner frequency.

The amplitude ratio of nearby earthquake pairs were used to remove the site response and propagation effects outside the near-source region (Fig. 1a). This was undertaken using a method similar to that of Lin & Shearer (2007), where near-source Vp/Vs was estimated using the ratios of differential arrival times for P and S-waves. Although Lin & Shearer's (2007) method assumes that the P and S-wave ray paths are the same, the method used to determine Q^{-1} in this study does not need the utility of this assumption. The method demonstrated in this study is also similar to that proposed by Matsumoto et al. (2009) to estimate Q^{-1} in the fault zone. A primary difference between these methods is that Matsumoto et al. (2009) incorporated the coda normalisation method (Aki, 1980) to eliminate source-effects in high frequency (>10 Hz). In contrast, the method used in this study focuses on near-source attenuation by only using nearby

(~1 km) earthquakes and the lower frequency range as opposed to source corner frequency. As such, the method does not need to model or cancel out source effects, making it much simpler and robust for modelling errors. Moreover, the accuracy of differential arrival time and amplitude ratio is substantially improved through the use of waveform cross-correlation.

2.2 Data and method

Seismic waveform data was used to estimate the attenuation structure near earthquake sources. Fig. 2(a) presents the distribution of earthquake hypocentres and seismic stations. The seismic network was comprised of seismic stations from Tohoku University, the Japan Meteorological Agency (JMA), and the National Research Institute for Earth Science and Disaster Resilience (NIED) Hi-net (NIED, 2019a) and V-net (NIED, 2019b). There were 2347 M2–3 earthquakes obtained from JMA's unified catalogue (https://www.data.jma.go.jp/svd/eqev/data/bulletin/hypo_e.html) between March 11, 2011 to December 31, 2016.

Only earthquake pairs with cross-correlation coefficients >0.8 for both P and S-waves were used from at least eight different stations for a frequency range from 2 to 5 Hz (49 852 pairs). The time-window length was set to 2.0 s; this is sufficiently shorter than the S-P time of waveform data, with the time-window beginning 0.3 s before the arrival times. Arrival times were either derived from the JMA unified catalogue or theoretically estimated based on the origin time and the hypocentre listed in the catalogue using the one-dimensional (1D) velocity structure model, JMA2001 (Ueno et al., 2002). A vertical component was used to estimate the Q^{-1} of the P-wave, while the transverse and radial components were used to estimate the Q^{-1} of the S-wave. The corner frequency of the P-wave may be presumed to be higher than that of the

S-wave (Hanks, 1981). Based on the fourth-order Butterworth filter, the frequency range was set to 2–4 Hz; sufficiently lower than source corner frequencies of the M2–3 earthquake S-waves (Yoshida et al., 2017), and thus P-waves. The central frequency (3 Hz) was used as f in Eq. (2), and the results from other frequency ranges were compared to the main result in Section 4.3.

To accurately quantify differential arrival times and accommodate for a narrow frequency range, amplitude ratios were measured in the time-domain using the principal component fit of aligned waveforms each time (Shelly et al., 2016), based on waveform cross-correlation. Data with low cross-correlation coefficients (cc <0.8) were discarded. Fig. 1(b) shows an example of comparing amplitude ratios, $A_{1\mathrm{i}}(f)/A_{2\mathrm{i}}(f)$, with the travel time differences, δt_{i}, for an earthquake pair, and Fig. 3 presents the waveforms used to compute $A_{1\mathrm{i}}(f)/A_{2\mathrm{i}}(f)$ and δt_{i} in Fig. 1(b). The decreasing pattern in $A_{1\mathrm{i}}(f)/A_{2\mathrm{i}}(f)$ with δt_{i} is clearly visible in Fig. 1(b), and other examples are shown in Fig S1.

To determine Q^{-1} of each earthquake pair, the mean of $\ln\frac{A_{1i}}{A_{2i}}$ and δt_{i} were subtracted from individual values and the best value of slope a was identified by fitting the linear equation $\ln\frac{A_1}{A_2} = a\delta t$. Here, the intercept was assumed as zero because of the subtraction of the mean values. Although the least squares method is available for this fitting, minimising the L1 norm residuals is more robust to outliers than minimising L2 norm residuals. In this study, a grid-search was used to determine the optimum a by changing the slope 1° in all possible ranges through the minimisation of the sum of L1-norm residuals of $\ln\frac{A_1}{A_2}$. Then, Q^{-1} was determined as $-a/\pi f$. To quantify the estimation error, 1000 estimations were produced based on bootstrap re-sampling of data (combinations of $\ln\frac{A_{1i}}{A_{2i}}$ and δt_{i}) for each earthquake pair; this provided the 95 % uncertainty range in the slope (Δθ). The Q^{-1} was quantified for an earthquake pair only when the used number of data was greater than eight for P-waves and 15 for S-waves. The mean residual of $\ln \frac{A_{1i}}{A_{2i}}$ (Fig. S2) was found to correlate well with Δθ. Finally, any results that satisfied any two conditions were discarded; (1) $\Delta\theta$ was large ($> 30°$ in the 95% confidence interval), or (2) the difference between the maximum and minimum δt was less than 0.4 s. This produced 2253 of 9407 results for P-wave and 3583 of 13457 results for S-waves.

Fig. 4(a)–(d) illustrates the frequency distributions of distances and time intervals of earthquake pairs with the near-source attenuation determined. The locations of hypocentres were taken from Yoshida & Hasegawa (2018). The median distance is 1.1 km, and the distances of most of earthquake pairs was closer than 2 km. The 95 % uncertainty range in the hypocentre locations was evaluated by recalculating the hypocentres 1000 times using the bootstrap resampling of differential arrival time data (Yoshida et al., 2020) and the same data and procedure as Yoshida & Hasegawa (2018). The median of the 95% confidence limits of the hypocentre locations was 0.018 and 0.027 km in the longitudinal and vertical directions, respectively (Fig. S3); these are much smaller than the distances of the event-pairs. Note that the method in this study does not use hypocentre information to estimateQ^{-1} itself, and as such, is unaffected by errors in the hypocentre determination.

Analysed earthquake pairs need to have similar focal mechanisms. Figs. 3(e) and (f) show the frequency distributions of the three-dimensional (3D) rotation angle of the focal mechanisms (Kagan, 1991) of earthquake pairs. The focal mechanism data was from Yoshida et al. (2019b), where estimation errors were < 30° in the 90 % confidence regions. The median of the 3D rotations angles were 17.4° and 15.7° for the P and S-waves, respectively.

2.3. Evaluation of unmodelled effects

The method used in this study did not consider the effects of differences in geometrical spreading and radiation pattern for earthquake pairs as these pairs are closely located and have similar focal mechanisms. However, slight differences in the effects of geometrical spreading and radiation pattern may impact upon the amplitude ratios and produce an apparent variation of near-source attenuation. These two effects were evaluated using hypocentre location and focal mechanism data from previous studies (Yoshida & Hasegawa, 2018; Yoshida et al., 2019b).

First, the synthetic amplitude ratio was computed from geometrical spreading and radiation pattern differences at each station for each event-pair by assuming that near-source attenuation was zero. Then, the same procedure described in Section 2.2 was applied to obtain the apparent values of near-source attenuation. As the synthetic amplitude ratio data is free from the effects of near-source attenuation, ideally the estimated Q^{-1} should be almost zero. However, differences in the radiation pattern and the geometrical spreading may potentially affect the apparent temporal variation. Yoshida et al. (2016) suggested that the focal mechanism diversity changes with time during swarm activity. The results from the synthetic data was compared to the results from real data in Section 3.

To estimate the effect of the geometrical spreading difference, Eq. (1) was used to produce the synthetic amplitude ratio data. This data was computed as $\frac{A_{1\mathrm{i}}}{A_{2\mathrm{i}}} = \frac{r_{2\mathrm{i}}^{\gamma}}{r_{1\mathrm{i}}^{\gamma}}$ for the same station combinations used to estimate near-source attenuation for each earthquake pair. Here, $r_{1\mathrm{i}}$ and $r_{2\mathrm{i}}$ is the distance from source-1 and source-2 to station- i, respectively. The hypocentre locations from Yoshida & Hasegawa (2018) were used, they relocated hypocentres precisely using the waveform correlation and the 1D velocity structure by Hasegawa et al. (1978) to estimate $r_{1\mathrm{i}}$ and $r_{2\mathrm{i}}$. An assumption that $\gamma = 1$ was adopted as direct waves were used for the analysis. To estimate the effect of the radiation pattern difference, moment tensors of earthquake pairs from

Yoshida et al. (2019b) were used with the equation from Dahm (1996) to compute amplitude ratio at each station.

3 Results

Figs. 5(a) and (b) present the frequency distributions for the Q^{-1}-values obtained for P and S-waves, respectively. At times, negative values were estimated when amplitude decay was unclear, although in most cases the values are positive (positive for 1951 of 2253 results for P-waves and 2259 of 3583 for S-waves). As the individual estimates are scattered, hereafter the characteristics of Q^{-1}-values were only statistically examined without discarding the negative values. Based on the 2000 bootstrap re-samplings of a simulated dataset of Q^{-1} values, the median P-wave was 0.050 with a 95 % uncertainty range between 0.046–0.051, and the median S-wave was 0.008 with a 95 % uncertainty range between 0.007–0.009.

Figs. 5, S1 and S2 present the results of applying the same method to the synthetic data. Figs. S4 and S5 are based on the synthetic data produced by separately considering the effects of differences in geometrical spreading and radiation patterns, respectively. Fig. 6 is based on the synthetic data considering both effects, and indicates that estimates of near-source attenuation are slightly positively biased (~0.02 for P-wave and ~0.006 for S-wave) because of these two effects. Ideally, the computed Q^{-1} from the synthetic data should be almost zero. Whilst the effects of geometrical spreading differences were found to be small, it systematically increases the estimate of Q^{-1}values (Fig. S4). The effects of the radiation pattern appear more random; however, they can have a more prominent impact on the estimates (Fig. S5). The median Q^{-1} estimated from real data, was significantly higher than the estimates from the synthetic data. This indicates that the method demonstrated in this study successfully retrieved information on actual near-source attenuation.

The Q^{-1}values were significantly different between an initial and later period of swarm activity for the P and S-waves. The median Q^{-1} for the P-wave in the initial ~50 days was 0.085 (with a 95 % confidence interval between 0.079–0.092), while the median in the later period (>50 days) was 0.044 (95 % uncertainty between 0.043–0.048). The median Q^{-1} for the S-wave was 0.025 (95 % uncertainty between 0.021–0.027) in the initial ~50 days, while the median was 0.005 (95 % uncertainty between 0.004–0.006) in the later period (>50 days). Thus, attenuation tends to be high in the initial swarm period than the later period. This tendency was not observed for the synthetic results (Figs. 6(a) and (b)), suggesting that this tendency was not produced by differences in geometrical spreading or radiation pattern, rather a reflection of the actual attenuation structure. The median Q^{-1} for the S-wave in the later period was almost the same as those of synthetic results, free from near-source attenuation. This indicates that near-source attenuation of the S-wave in the later period was too small to be detected by the method used in this study, despite detection of the high Q^{-1}value in the initial period.

To visualise the temporal variation of Q^{-1} in further detail, the median Q^{-1} at even 5 day intervals from the initiation of swarm activity was determined. It was assumed that the obtained Q^{-1} value essentially represents an average between the occurrence timings of two earthquakes. The Q^{-1} values were allocated to all temporal points between the timing of the two earthquakes. The median was obtained at each point when the number of individual estimates was greater than or equal to 10. The 95 % uncertainty range was computed using the 2000 bootstrap re-samplings of a simulated dataset of Q^{-1} values at each temporal point. Figs. 5(c) and (d) show the temporal variations of Q^{-1} for P and S-waves, respectively. Whilst individual values vary over a wide range, their median values exhibit a characteristic temporal variation; they were high in the initial period (<50 days) and decreased, becoming almost constant in the later period for both P and S-waves.

Figs. 6(c) and (d) present the temporal variations of Q^{-1} for P and S-waves computed from the synthetic data, respectively. The temporal variations of synthetic results were mainly a result of the differences in the radiation pattern (Figs. S5(c) and (d)), rather than the geometrical spreading (Figs. S4(c) and (d)). Although the median appears to have some temporal variations, the amplitudes are smaller than those obtained for real data. The difference between the results from the real and synthetic data indicates that the temporal variations of Q^{-1} for the former are a result of an actual variation of Q^{-1}.

The temporal pattern of Q^{-1} appears to be correlated with those of source and seismicity parameters, including fault strength, background seismicity rate, stress drop, and b-value (Figs. 2(b)–(e)), which were independently estimated. Fault strength (shear stress magnitude with the occurrence of slip) and stress drop were low during the initial period (~50 days after the earthquake), then increased to be almost constant in the later period (Figs. 2(b) and (d)). Seismicity rate and b-value were high in the initial period, and then decreased to be almost constant in the later period (Figs. 2(c) and (e)). Their values were abnormal during the initial period (<50 days), and changed to almost constant, typical values; this tendency is similar to temporal changes in Q^{-1} values from this study.

All of these parameters are related to the presence of fluids; fault strength is proportional to effective normal stress and has an inverse relationship with pore pressure. The background seismicity rate may be presumed to reflect external forces, which may include an increase in pore pressure (Hainzl & Ogata, 2005; Roland & McGuire, 2009; Llenos et al., 2009; Llenos &

Michael, 2013). Stress drops and b-values have also been reported to have an inverse and a direct relationship with pore pressure, respectively (Wyss, 1973; Bachmann et al., 2011, 2012; Allmann and Shearer, 2007; Chen and Shearer, 2011; Goertz-Allmann et al., 2011). These synchronised temporal variations suggest that pore pressure was high during the initial swarm stage and decreased over time, with the temporal evolution affecting the source and seismicity characteristics of the swarm. Moreover, Q^{-1}, in the intrinsic and the scattering attenuations, is expected to increase with the presence of fluids (Winkler & Nur, 1982). By assuming that the temporal variation in Q^{-1} reflects the change in intrinsic Q^{-1}, the observed temporal change may also be attributed to the pore pressure change together with temporal changes in other source and seismicity parameters.

It was estimated that the swarm activity was triggered by a pore pressure increase after the 2011 Tohoku-Oki earthquake (Terakawa et al., 2013; Yoshida et al., 2016). The E–W extensional stress and the dynamic shaking caused from the Tohoku-Oki earthquake, facilitated the ascent of fluids immediately below the source area of the swarm, generating considerable pore pressure increase in the source area during the initial stage. The fluid diffusion indicated by the hypocentre migration in swarm activity caused pore pressure to decrease over time. The temporal pattern of Q^{-1}, together with the patterns in the fault strength, stress drop, background seismicity rate, and b-value, are consistent with this hypothesis.

The Q^{-1} values of the P-wave tended to be higher than those of the S-waves; these results are similar to those obtained for frequencies higher than 1 Hz in various regions of the world (Sato et al., 2012). This relationship is contrary to what was expected, based on theoretical considerations in a simple model of intrinsic absorption (Knopoff, 1971). This relationship may be explained by including the contribution of crustal pore fluids to the attenuation of seismic waves as suggested by Hauksson & Shearer (2006), or the effects of scattering attenuation.

The method used in this study successfully detected a high attenuation anomaly in the initial period of the swarm, predicted by the fluid-diffusion model proposed in previous studies (Yoshida et al., 2016, 2017, 2019b; Yoshida & Hasegawa, 2018). Monitoring Q^{-1} at seismogenic depths would help in understanding the states of potential seismogenic zones and the occurrence mechanism for earthquakes.

4 Discussion

4.1 Spatial distribution of near-source attenuation

This study obtained the temporal variation for Q^{-1} values in the source region of the Yamagata-Fukushima border swarm. However, as the location of swarm activity change with time (Okada et al., 2015; Yoshida & Hasegawa, 2018), it is possible that the temporal change may be an artefact due to the spatial change in Q^{-1}.

To quantify the spatial variation of Q^{-1}, the mean of Q^{-1} at evenly spaced $200 \times 200 \times 200$ points were computed to divides the entire region in latitude (37.63–37.85°), longitude (139.885–140.045°), and depth (4.0–14.0 km). The obtained Q^{-1}value was assumed to essentially represent an average value within the sphere where the diameter is the distance of the two earthquakes and the centre is the mean location (Fig. 1(a)). Relocated hypocentres by Yoshida & Hasegawa (2018) were used for the locations of earthquake pairs, and Q^{-1} values were allocated to all points within the sphere. The mean values were quantified at the point only when the number of individual estimates was greater than or equal to 5; at this point, the spatial variation of Q^{-1} for the P-wave was determined.

The quantified spatial variation of Q^{-1} for the P-wave is shown in Figs. 7(a)–(d) at depths of 7.2, 7.8, 8.4 and 9.0 km in map views and Fig. 8 in cross-sectional views. They have a lateral variation; Q^{-1} tends to be high in the central part of the focal region and lower in the surrounding area. Hypocentre locations in the initial stage are highlighted in red in Figs. 7(e)–(f), appearing to correspond to locations with a high Q^{-1}. Previous studies reported synchronised temporal variations in fault strength (Yoshida et al., 2016), stress drops (Yoshida et al., 2017, 2019b), b-value (Yoshida et al., 2017), and background seismicity rates (Yoshida & Hasegawa, 2018) (Fig. 2(b)–(e)). These synchronised changes were estimated to reflect the diffusion of pore pressure, in particular, high pore pressure during the initial stage and its temporal decrease (Yoshida et al., 2017). These observations appear may be better explained by the potential that the spatial variation of Q^{-1} actually reflects its temporal variation combined with the migration behaviour of hypocentres from pore pressure diffusion.

4.1. Potential for artificial variations in source-effect due to variation of near-source attenuation

Seismic waveform records from an earthquake contain information on the source and the Earth's structure. The correct separation of source and propagation effects is vital to examine the earthquake source and structure. One important factor to successfully separate the source effect is the potential for strong near-source attenuation. Dismissal of this attenuation may lead to a systematic source-effect estimation error (Abercrombie, 2015).

Two types of methods exist to extract information regarding earthquake source; (1) empirical methods using waveforms of nearby earthquakes, such as Green's function (Empirical Green's Function (EGF) method; Hartzell, 1978), and (2) theoretical methods using simultaneously or independently estimated propagation and site-effects, based on physical models (Andrew, 1986; Takahashi et al., 2005). Path and site-effects are likely to be most effectively eliminated by EGF methods that use waveforms of a nearby earthquake as Green's function (hereafter the nearby event is referred as the EGF event). However, even results of EGF methods would be affected by ignoring near-source attenuation if the distance between the two events becomes larger. Previous studies have shown that the source corner frequency determined using EGF methods is affected by the distance between the two events (Kane et al., 2013; Abercrombie, 2015). To avoid this, it is important to confirm that EGF events are sufficiently close to the target earthquake and/or consider the effect of near-source attenuation.

For the Yamagata-Fukushima border swarm, the average stress drop of small earthquakes change with time almost synchronously with near-source attenuation (Figs. 2(d) and 5). Although temporal variation can be explained by assuming that both parameters were affected by the temporal change in pore pressure, another possibility is that the temporal change in the source parameter may be an artefact of dismissing changes in near-source attenuation or vice versa. As this study has verified that the obtained temporal pattern of near-source attenuation was not controlled by source-effects (differences in rupture process, frequency content, and focal mechanism), I here consider the latter possibility that the temporal change in stress drop is an artefact of the ignorance of changes in near-source attenuation

Yoshida et al. (2017, 2019b) estimated stress drops for small earthquakes in this swarm using different three methods and obtained consistent results. Yoshida et al. (2017) first estimated frequency dependent Q^{-1} values and site-effects based on the coda normalisation method (Aki, 1980; Philipps & Aki, 1986), using the results to retrieve the source effects. As they assumed that Q^{-1} was homogeneous in space and time, the estimated source-effects in this approach may have been affected by the change in near-source attenuation. However, Yoshida et al. (2017) obtained a similar temporal variation of stress drop based on the EGF method using S-coda waves, effectively excluding the effects of near-source attenuation (Mayeda et al, 2007). Moreover, Yoshida et al. (2019b) obtained a similar temporal variation also based on the EGF method using direct S-waves from very close earthquakes (<0.5 km) as Green's functions; this is also not as susceptible to the effects of near-source attenuation. As all three results show similar temporal patterns of stress drops, it is reasonable to consider that changes in stress drop are not an artefact. Whilst it is difficult to completely deny the potential that the results are to some extent, affected by changes in near-source attenuation over time, it is reasonable to consider that stress drops of small earthquakes in the source region of this swarm actually changed with time following the 2011 Tohoku-Oki earthquakes.

4.2. Frequency-dependence of near-source attenuation

Insights into the frequency dependence of Q^{-1} are required to evaluate the effects of near-source attenuation on source-effect estimation. The near-source Q^{-1} values were estimated for frequency ranges between 1–2 and 4–8 Hz, in the same way as the results for 2–4 Hz. The frequency distribution of Q^{-1} values are shown in Figs. 9(a)–(d). The median and the 95 % confidence intervals for Q^{-1} are summarised in Table 1. There were 1823 and 2067 results for the frequency ranges of 1–2 and 4–8 Hz for the P-wave, respectively. There were 1308 and 2876 results for the frequency ranges of 1–2 and 4–8 Hz for the S-wave, respectively.

The median Q^{-1} for the P-wave was 0.102 (with a 95 % confidence interval of 0.099–0.106) and 0.032 (with a 95 % confidence interval of 0.029–0.03) for the frequency ranges of 1–2 and 4–8 Hz, respectively. The median Q^{-1} for the S-wave was 0.035 (with a 95 % confidence interval of 0.030–0.036) and 0.004 (95 % confidence interval of 0.003–0.005) for the frequency ranges of 1–2 and 4–8 Hz, respectively. The Q^{-1} values obtained tend to decrease with frequency as a whole; 0.102, 0.050 and 0.032 in the frequency ranges of 1–2, 2–4, and 4–8 Hz for the P-wave, respectively, and 0.035, 0.008, and 0.004 in the frequency range of 1–2, 2–4, 4–8 Hz for the S-wave, respectively. This decreasing tendency with frequency holds both in the initial and the later periods and is similar to results of previous studies for frequencies above 1 Hz (Sato et al., 2012). However, the decay rate of Q^{-1} for the S-wave is somewhat complex; it abruptly decreases from 1–2 to 2–4 Hz, and then only slightly decreases from 2–4 to 4–8 Hz.

The temporal changes of the median values are shown in Figs. 9(e)–(h), in which the values were computed for each time bin. With the exception of the results for the 1–2 Hz frequency range of the S-wave, the Q^{-1} values change with time similar to those of 2–4 Hz. The values were high in the initial period (<50 days), then decreased to be constant in the later period. The temporal patterns are consistent with the hypothesis that temporal change in pore pressure affects the anelastic and scattering property in the source region of the present swarm. The temporal pattern of Q^{-1} in the 1–2 Hz range of the S-wave was more complex and differs from others. It is difficult to know exactly the cause of this different temporal pattern and the complex frequency dependence of Q^{-1}. The Q^{-1} values obtained were affected by intrinsic absorption and scattering losses. The frequency dependence of intrinsic attenuation and scattering attenuation is different (Sato et al., 2012), and the combination of the two effects may account for the complicated frequency dependence. It is likely that fluid flow within the fracture network affects high-frequency waveforms (Guo et al., 2018). The complicated frequency dependence may include information such as the spatial extent and the shape of pores and cracks filled by fluid.

4.3 Estimation of near-source attenuation through consideration of the effects of geometrical spreading and radiation pattern

Differences in the geometrical spreading and radiation pattern of earthquake pairs affect the estimation of near-source Q^{-1}. Although this effect is minor in this study (Fig. 6), the effect makes it difficult to interpret their absolute values. The method used in this study is able to avoid the effects of differences in geometrical spreading and radiation pattern if precise hypocentre location data and focal mechanisms data are available. In this case, near-source attenuation was estimated by incorporating the effects of differences in geometrical spreading and radiation pattern. Note that this estimation was somehow affected by estimation errors of relative hypocentre locations and focal mechanisms.

The theoretical amplitude ratios originating from the differences in the geometrical spreading and radiation pattern quantified in Section 2.3 were utilised. First, the observed amplitude ratios were multiplied by the inverse of corresponding theoretical amplitude ratios to remove the effects of geometrical spreading and radiation pattern. Then, the same method to compute near-source Q^{-1} for each earthquake pair in the main result was applied. Fig. 10 shows the resulting estimated near-source attenuation. The Q^{-1} values were 0.013 (with 95 % confidence interval of 0.012–0.015) for the P-wave and 0.008 (95 % confidence interval of 0.007–0.009) for the S-wave; these are lower than those in Section 3. This may largely be attributed to ignoring the effects of geometrical spreading and radiation pattern which systematically increased the estimates of Q^{-1} (Fig. 6). The median Q^{-1}-values were significantly positive even if the effects of differences in geometrical spreading and radiation pattern were removed. The temporal pattern of Q^{-1} was still similar to those in the previous section (Section 3) (Fig. 5) and the temporal patterns of fault frictional strength, background seismicity rate, stress drop, and b-value (Figs. 2(b)–(e)).

Yoshida et al. (2017) used the coda normalisation method to estimate $Q^{-1}$for the S-wave in the surrounding crust of the Yamagata-Fukushima swarm region, obtaining ~0.005–~0.01 in the 2–4 Hz frequency range; their estimates are comparable to those obtained in this study. According to the temporal variation in Fig. 10(d), the Q^{-1} value in some time bins during the initial period (<50 days) was significantly higher than this range, suggesting that pore pressure is higher near earthquake sources than in the surrounding crust during this period.

5. Conclusions

This study examined near-source attenuation in the focal region of intense swarm activity in the Yamagata-Fukushima border region of Japan. This was considered to have been triggered by fluid movement following the 2011 Tohoku-Oki earthquake (Terakawa et al., 2013; Yoshida et al., 2016). Near-source attenuation was estimated using a new technique that precisely determines the decay of the amplitude ratios for two nearby earthquakes with travel time differences using similar waveforms. Whilst the obtained Q^{-1} values vary over a wide range, their median values exhibit characteristic temporal variation; Q^{-1} was large for the initial ~50 days, and significantly decreased, becoming almost constant after 50 days. These temporal patterns are similar to those independently obtained for background seismicity rates, b-values, stress drops, and fault strength. The synchronous change suggests that swarm was triggered by fluid movement following the 2011 Tohoku-Oki earthquake, and source and seismicity characteristics and seismic attenuation were affected by pore pressure.

This results from this study suggest that seismic attenuation intensity is higher near the earthquake source than in the surrounding crust in some situations. Localised higher attenuation near the source produces a systematic estimation error of earthquake source effects; the attenuation is erroneously estimated as a part of the earthquake source signal. It is therefore important to examine the intensity and the frequency dependence of near-source attenuation to accurately estimate earthquake source properties.

The method used in this study cannot handle frequency ranges higher than the source corner frequency. It is necessary to understand attenuation behaviour at frequencies > 8 Hz, as it is closely related to estimating source parameters for small earthquakes. The estimation of near-source attenuation at higher frequency ranges would be possible in future research by analysing waveform data from smaller earthquakes (M<2) using dense temporary seismic network data.

Acknowledgments and data

This study used hypocentres and P and S-wave arrival time data reported in the unified catalogue of the Japan Meteorological Agency (JMA). The seismograms were collected and stored by JMA, national universities, and NIED (http://www.hinet.bosai.go.jp/?LANG=en). The figures were created using GMT (Wessel and Smith, 1998). I thank Kentaro Emoto for discussions on scattering attenuation, Genti Toyokuni for discussions on intrinsic attenuation, Masaoki Uno for discussions on the pore pressure state in the fault zone, and Satoshi Matsumoto for discussions on the effects of radiation pattern. This research was supported by JSPS KAKENHI Grant Number JP 20K14569.

References

Abercrombie, R.E. (2015) Investigating uncertainities in empirical Green's function analysis of earthquake source parameters. J. Geophys. Res. Earth, 4263–4277. doi:10.1002/2015JB011984.

Aki, K. (1967) Scaling law of seismic spectrum. J. Geophys. Res., 72, 1217–1231, Wiley Online Library.

Aki, K. (1980) Attenuation of shear-waves in the lithosphere for frequencies from 0.05 to 25 Hz. Phys. Earth Planet. Inter., 21, 50–60, Elsevier.

Allmann, B.P. & Shearer, P.M. (2007) Spatial and temporal stress drop variations in small earthquakes near Parkfield, California. J. Geophys. Res. Solid Earth, 112, 1–17. doi:10.1029/2006JB004395

Andrews, D.J. (1986) Objective determination of source parameters and similarity of earthquakes of different size. Earthq. source Mech., 37, 259–267, Wiley Online Library.

Bachmann, C.E., Wiemer, S., Woessner, J. & Hainzl, S. (2011) Statistical analysis of the induced Basel 2006 earthquake sequence: Introducing a probability-based monitoring approach for Enhanced Geothermal Systems. Geophys. J. Int., 186, 793–807. doi:10.1111/j.1365-246X.2011.05068.x

Chen, X. & Shearer, P.M. (2011) Comprehensive analysis of earthquake source spectra and swarms in the Salton Trough, California. J. Geophys. Res. Solid Earth, 116, 1–17. doi:10.1029/2011JB008263

Dahm, T. (1996) Relative moment tensor inversion based on ray theory: theory and synthetic tests. Geophys. J. Int., 124, 245–257, Blackwell Publishing Ltd Oxford, UK.

Goertz-Allmann, B.P., Goertz, A. & Wiemer, S. (2011) Stress drop variations of induced earthquakes at the Basel geothermal site. Geophys. Res. Lett., 38, doi:10.1029/2011GL047498

Guo, J., Shuai, D., Wei, J., Ding, P. & Gurevich, B. (2018) P-wave dispersion and attenuation due to scattering by aligned fluid saturated fractures with finite thickness: Theory and experiment. Geophys. J. Int., 215, 2114–2133, Oxford University Press.

Hainzl, S. & Ogata, Y. (2005) Detecting fluid signals in seismicity data through statistical earthquake modeling. J. Geophys. Res. Solid Earth, 110, 1–10. doi:10.1029/2004JB003247

Hartzell, S.H. (1978) Earthquakes aftershocks as Green's Functions. Geophys. Res. Lett., 5, doi:10.1029/GL005i001p00001

Hanks, T.C. (1981) The corner frequency shift, earthquake source models, and Q. Bull. Seismol. Soc. Am., 71, 597–612, The Seismological Society of America.

Hasegawa, A., Nakajima, J., Umino, N. & Miura, S. (2005) Deep structure of the northeastern Japan arc and its implications for crustal deformation and shallow seismic activity. Tectonophysics, 403, 59–75. doi:10.1016/j.tecto.2005.03.018

Hauksson, E. & Shearer, P.M. (2006) Attenuation models (QP and QS) in three dimensions of the southern California crust: Inferred fluid saturation at seismogenic depths. J. Geophys. Res. Solid Earth, 111, Wiley Online Library.

Hubbert, M.K. & Rubey, W.W. (1959) Role of fluid overpressure in the mechanics of overthrust faulting. Geol. Soc. Am. Bull., 70, 167–206. doi:10.1130/0016-7606(1959)70

Kagan, Y.Y. (1991) 3-D rotation of double-couple earthquake sources. Geophys. J. Int., 106, 709–716, Blackwell Publishing Ltd Oxford, UK.

Kane, D.L., Kilb, D.L. & Vernon, F.L. (2013) Selecting empirical Green's functions in regions of fault complexity: A study of data from the San Jacinto fault zone, southern California. Bull. Seismol. Soc. Am., 103, 641–650, Seismological Society of America.

Kaneko, Y. & Shearer, P.M. (2014) Seismic source spectra and estimated stress drop derived from cohesive-zone models of circular subshear rupture. Geophys. J. Int., 197, 1002–1015. doi:10.1093/gji/ggu030

Knopoff, L. (1971) Attenuation, in mantle and core in planetary physics, Elsevier.

Kriegerowski, M., Cesca, S., Ohrnberger, M., Dahm, T. & Krüger, F. (2019) Event couple spectral ratio Q method for earthquake clusters: application to northwest Bohemia. Solid Earth, 10, 317–328, Copernicus GmbH.

Lin, G. & Shearer, P. (2007) Estimating local Vp/Vs ratios within similar earthquake clusters. Bull. Seismol. Soc. Am., 97, 379–388. doi:10.1785/0120060115

Llenos, A.L., McGuire, J.J. & Ogata, Y. (2009) Modeling seismic swarms triggered by aseismic transients. Earth Planet. Sci. Lett., 281, 59–69, Elsevier B.V. doi:10.1016/j.epsl.2009.02.011

Llenos, A.L. & Michael, A.J. (2013) Modeling earthquake rate changes in Oklahoma and Arkansas: Possible Signatures of induced seismicity. Bull. Seismol. Soc. Am., 103, 2850–2861. doi:10.1785/0120130017

Matsumoto, S., Uehira, K., Watanabe, A., Goto, K., Iio, Y., Hirata, N., Okada, T., et al. (2009) High resolution Q- 1 estimation based on extension of coda normalization method and its application to P-wave attenuation structure in the aftershock area of the 2005 West Off Fukuoka Prefecture Earthquake (M 7.0). Geophys. J. Int., 179, 1039–1054, Blackwell Publishing Ltd Oxford, UK.

Mayeda, K., Malagnini, L. & Walter, W.R. (2007) A new spectral ratio method using narrow band coda envelopes: Evidence for non-self-similarity in the Hector Mine sequence. Geophys. Res. Lett., 34, 2–6. doi:10.1029/2007GL030041

Mindaleva, D., Uno, M., Higashino, F., Nagaya, T., Okamoto, A. & Tsuchiya, N. (2020) Rapid fluid infiltration and permeability enhancement during middle--lower crustal fracturing: Evidence from amphibolite--granulite-facies fluid--rock reaction zones, Sør Rondane Mountains, East Antarctica. Lithos, 105521, Elsevier.

Nakajima, J. & Matsuzawa, T. (2017) Anelastic properties beneath the Niigata--Kobe tectonic zone, Japan. Earth, Planets Sp., 69, 1–9, SpringerOpen.

National Research Institute for Earth Science and Disaster Resilience (2019a) NIED Hi-net. Natl. Res. Inst. Earth Sci. Disaster Resil.,doi:10.17598/NIED.0003

National Research Institute for Earth Science and Disaster Resilience (2019b) NIED V-net. Natl. Res. Inst. Earth Sci. Disaster Resil., doi:10.17598/NIED.0006

Nur, A. & Booker, J.R. (1972) Aftershocks caused by pore fluid flow? Science (80-.)., 175, 885–887. doi:10.1126/science.175.4024.885

Okada, T., Matsuzawa, T., Umino, N., Yoshida, K., Hasegawa, A., Takahashi, H., Yamada, T., et al. (2016) Hypocenter migration and crustal seismic velocity distribution observed for the inland earthquake swarms induced by the 2011 Tohoku-Oki earthquake in NE Japan: Implications for crustal fluid distribution and crustal permeability. in Crustal Permeability. doi:10.1002/9781119166573.ch24

Phillips, W.S. & Aki, K. (1986) Site amplification of coda waves from local earthquakes in central California. Bull. Seismol. Soc. Am., 76, 627–648, The Seismological Society of America.

Poupinet, G., Ellsworth, W.L. & Frechet, J. (1984) Monitoring velocity variations in the crust using earthquake doublets: An application to the Calaveras Fault, California. J. Geophys. Res. Solid Earth, 89, 5719–5731, Wiley Online Library.

Roland, E. & McGuire, J.J. (2009) Earthquake swarms on transform faults. Geophys. J. Int., 178, 1677–1690. doi:10.1111/j.1365-246X.2009.04214.x

Sato, H., Fehler, M.C. & Maeda, T. (2012) Seismic wave propagation and scattering in the heterogeneous earth, Vol. 496, Springer.

Shapiro, S.A., Huenges, E. & Borm, G. (1997) Estimating the crust permeability from fluid-injection-induced seismic emission at the KTB site. Geophys. J. Int., 131. doi:10.1111/j.1365-246X.1997.tb01215.x

Shelly, D.R., Ellsworth, W.L. & Hill, D.P. (2016) Fluid-faulting evolution in high definition: Connecting fault structure and frequency-magnitude variations during the 2014 Long Valley Caldera, California, earthquake swarm. J. Geophys. Res. Solid Earth, 121, 1776–1795. doi:10.1002/2015JB012719

Sibson, R.H. (1992) Implications of fault-valve behaviour for rupture nucleation and recurrence. Tectonophysics, 211, 283–293. doi:10.1016/0040-1951(92)90065-E

Takahashi, T., Sato, H., Ohtake, M. & Obara, K. (2005) Scale dependence of apparent stress for earthquakes along the subducting pacific plate in northeastern Honshu, Japan. Bull. Seismol. Soc. Am., 95, 1334–1345. doi:10.1785/0120040075

Takahashi, T., Sato, H., Ohtake, M. & Obara, K. (2005) Scale dependence of apparent stress for earthquakes along the subducting pacific plate in northeastern Honshu, Japan. Bull. Seismol. Soc. Am., 95, 1334–1345. doi:10.1785/0120040075

Terakawa, T., Hashimoto, C. & Matsu'ura, M. (2013) Changes in seismic activity following the 2011 Tohoku-oki earthquake: Effects of pore fluid pressure. Earth Planet. Sci. Lett., 365, 17–24. doi:10.1016/j.epsl.2013.01.017

Ueno, H., Hatakeyama, S., Aketagawa, T., Funasaki, J. & Hamada, N. (2002) Improvement of hypocenter determination procedures in the Japan Meteorological Agency. Q. J. Seism., 65, 123–134.

Wcisło, M., Eisner, L., Málek, J., Fischer, T., Vlček, J. & Kletetschka, G. (2018) Attenuation in West Bohemia: Evidence of High Attenuation in the Nov{\`y} Kostel Focal Zone and Temporal Change Consistent with CO2 DegassingAttenuation in West Bohemia. Bull. Seismol. Soc. Am., 108, 450–458, GeoScienceWorld.

Wessel, P. & Smith, W.H.F. (1998) New, improved version of generic mapping tools released. Eos, Trans. Am. Geophys. Union, 79, 579–579. doi:10.1029/98EO00426

Winkler, K.W. & Nur, A. (1982) Seismic attenuation: Effects of pore fluids and frictional-sliding. Geophysics, 47, 1–15, Society of Exploration Geophysicists.

Wyss, M. (1973) Towards a Physical Understanding of the Earthquake Frequency Distribution. Geophys. J. R. Astron. Soc., 31, 341–359. doi:10.1111/j.1365-246X.1973.tb06506.x

Yoshida, K. & Hasegawa, A. (2018) Hypocenter Migration and Seismicity Pattern Change in the Yamagata-Fukushima Border, NE Japan, Caused by Fluid Movement and Pore Pressure Variation. J. Geophys. Res. Solid Earth, 123, 5000–5017. doi:10.1029/2018JB015468

Yoshida, K., Hasegawa, A., Okada, T., Iinuma, T., Ito, Y. & Asano, Y. (2012) Stress before and after the 2011 great Tohoku-oki earthquake and induced earthquakes in inland areas of eastern Japan. Geophys. Res. Lett., 39. doi:10.1029/2011GL049729

Yoshida, K., Hasegawa, A. & Yoshida, T. (2016) Temporal variation of frictional strength in an earthquake swarm in NE Japan caused by fluid migration. J. Geophys. Res. Solid Earth, 121, 5953–5965. doi:10.1002/2016JB013022

Yoshida, K., Saito, T., Urata, Y., Asano, Y. & Hasegawa, A. (2017) Temporal Changes in Stress Drop, Frictional Strength, and Earthquake Size Distribution in the 2011 Yamagata-Fukushima, NE Japan, Earthquake Swarm, Caused by Fluid Migration. J. Geophys. Res. Solid Earth, 122, 10,379-10,397. doi:10.1002/2017JB014334

Yoshida, K., Hasegawa, A., Yoshida, T. & Matsuzawa, T. (2019a) Heterogeneities in stress and strength in tohoku and its relationship with earthquake sequences triggered by the 2011 M9 Tohoku-Oki earthquake. Pure Appl. Geophys., 176, 1335–1355, Springer.

Yoshida, K., Saito, T., Emoto, K., Urata, Y. & Sato3, D. (2019b) Rupture directivity, stress drop, and hypocenter migration of small- and moderate-sized earthquakes in the Yamagata-Fukushima border swarm triggered by upward pore-pressure migration after the 2011 Tohoku-Oki earthquake. Tectonophysics, 769, 228184.

Yoshida, K., Taira, T., Matsumoto, Y., Saito, T., Emoto, K. & Matsuzawa, T. (2020) Stress Release Process Along an Intraplate Fault Analogous to the Plate Boundary: A Case Study of the 2017 M5.2 Akita-Daisen Earthquake, NE Japan. J. Geophys. Res. Solid Earth, 125. doi:10.1029/2020JB019527

Tables

Table 1. Median of Q^{-1} values and the 95 % confidence interval.

Frequency	phase	Data	Q^{-1} -value			Figure	Notes
			entire period	initial period	later period		
1-2 Hz	P	real data	0.102 (0.099-0.106)	0.200 (0.184-0.228)	0.096 (0.091-0.099)	Fig. 9a	
2-4 Hz	P	real data	0.050 (0.046-0.051)	0.085 (0.079-0.092)	0.044 (0.043-0.046)	Fig. 6a	
4-8 Hz	P	real data	0.032 (0.029-0.033)	0.054 (0.052-0.060)	0.028 (0.026-0.029)	Fig. 9b	
2-4 Hz	P	real data	0.013 (0.012-0.015)	0.037 (0.029-0.043)	0.012 (0.011-0.013)	Fig. 10a	geometrical spreading and radiation pattern
2-4 Hz	P	synthetic	0.010 (0.010-0.010)	0.010 (0.009-0.010)	0.010 (0.010-0.010)	Fig. S4a	geometrical spreading
2-4 Hz	P	synthetic	0.016 (0.014-0.018)	0.007 (0.002-0.014)	0.017 (0.015-0.020)	Fig. S5a	radiation pattern
2-4 Hz	P	synthetic	0.025 (0.022-0.027)	0.016 (0.012-0.020)	0.026 (0.025-0.028)	Fig. 7a	geometrical spreading and radiation pattern
1-2 Hz	S	real data	0.035 (0.030-0.036)	0.028 (0.021-0.036)	0.035 (0.030-0.039)	Fig. 9c	
2-4 Hz	S	real data	0.008 (0.007-0.009)	0.025 (0.021-0.027)	0.006 (0.006-0.007)	Fig. 6b	
4-8 Hz	S	real data	0.004 (0.03-0.05)	0.021 (0.019-0.026)	0.003 (0.002-0.003)	Fig. 9d	
2-4 Hz	S	real data	0.008 (0.007-0.008)	0.011 (0.009-0.013)	0.007 (0.006-0.008)	Fig. 10b	geometrical spreading and radiation pattern
2-4 Hz	S	synthetic	0.006 (0.006-0.006)	0.006 (0.006-0.006)	0.006 (0.006-0.006)	Fig. S4b	geometrical spreading
2-4 Hz	S	synthetic	-0.003 (-0.004- -0.002)	0.000 (-0.002- 0.002)	-0.003 (-0.004- -0.002)	Fig. S5b	radiation pattern
2-4 Hz	S	synthetic	0.006 (0.005-0.006)	0.007 (0.006-0.009)	0.006 (0.005-0.006)	Fig. 7b	geometrical spreading and radiation pattern

Figures

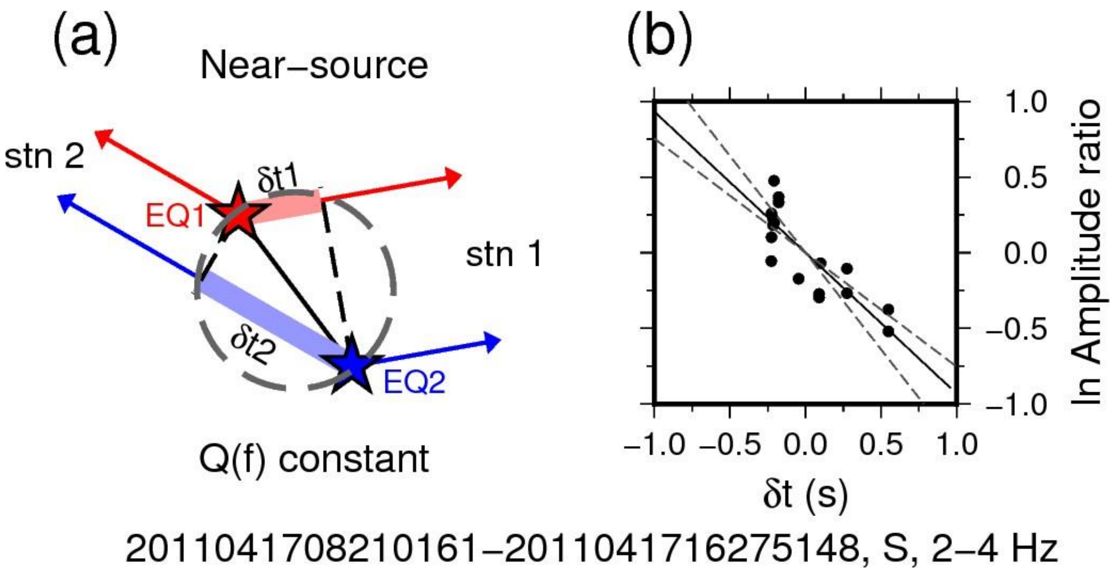

Figure 1. (a) A schematic of the principle underpinning near-source attenuation estimation. Stars and arrows show the locations of the earthquake pairs and the ray paths, respectively. Note that the method does not assume plane wave approximation; (b) an example of the relationship between amplitude ratios, $\boldsymbol{A_{1\mathrm{i}}(f)/A_{2\mathrm{i}}(f)}$, and differential arrival times, $\boldsymbol{\delta t_{\mathrm{i}}}$, of an earthquake

pair. The solid line denotes the best-fit slope. The broken lines show the upper and lower slope estimates in the 95 % confidence region.

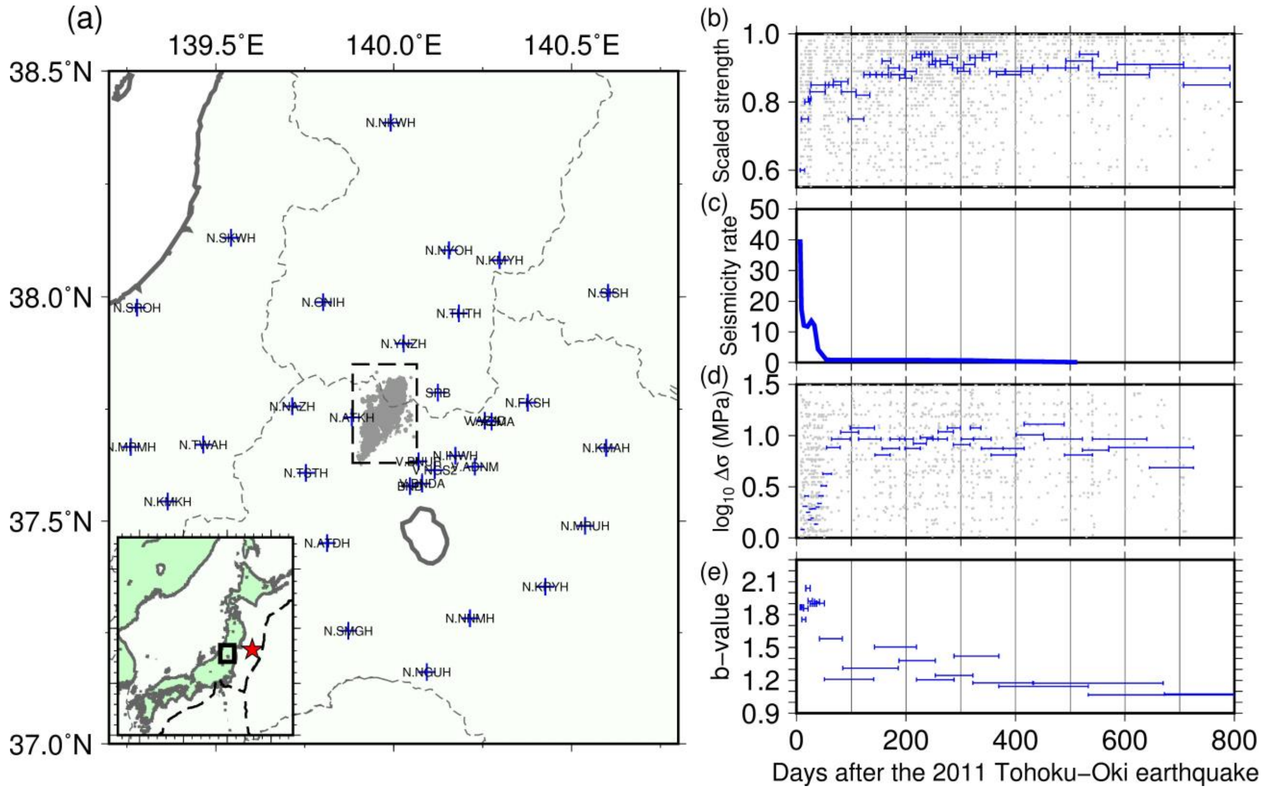

Figure 2. (a) Distribution of hypocentres (grey circles) and seismic stations (blue crosses) in the study area. In the inset, the range of the hypocentre is the bold rectangle, the red star indicates the hypocentre of the 2011 M9 Tohoku-Oki earthquake, and the broken curve shows the trench; (b), (c), (d) and (e) temporal variations in fault frictional strength scaled by the maximum shear stress (Yoshida et al., 2016), background seismicity rate (Yoshida & Hasegawa, 2018), stress drop (Yoshida et al., 2019b), and b-value (Yoshida et al., 2017), respectively. In (b) and (d), individual results and geometric means are shown by grey circles and blue lines, respectively.

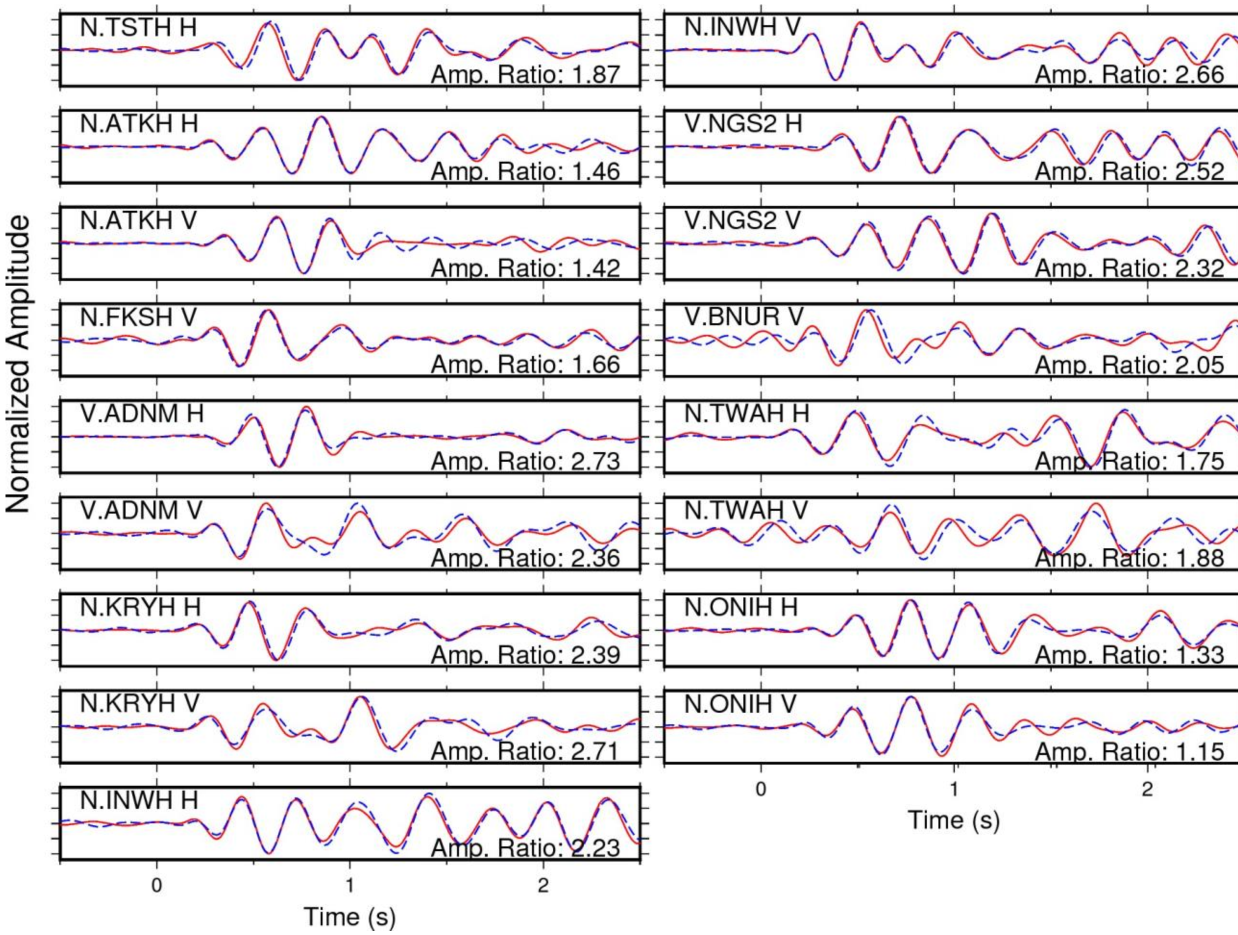

Figure 3. Waveforms of the event-pair in Fig. 1 (b) used to estimate near-source attenuation. Red solid and blue broken traces show the waveforms of event-1 and event-2, respectively. The timing was adjusted by waveform correlation. The maximum amplitude of the waveforms were normalised. Numbers on the lower right denote the amplitude ratios, and letters on the upper left denote the station names and components.

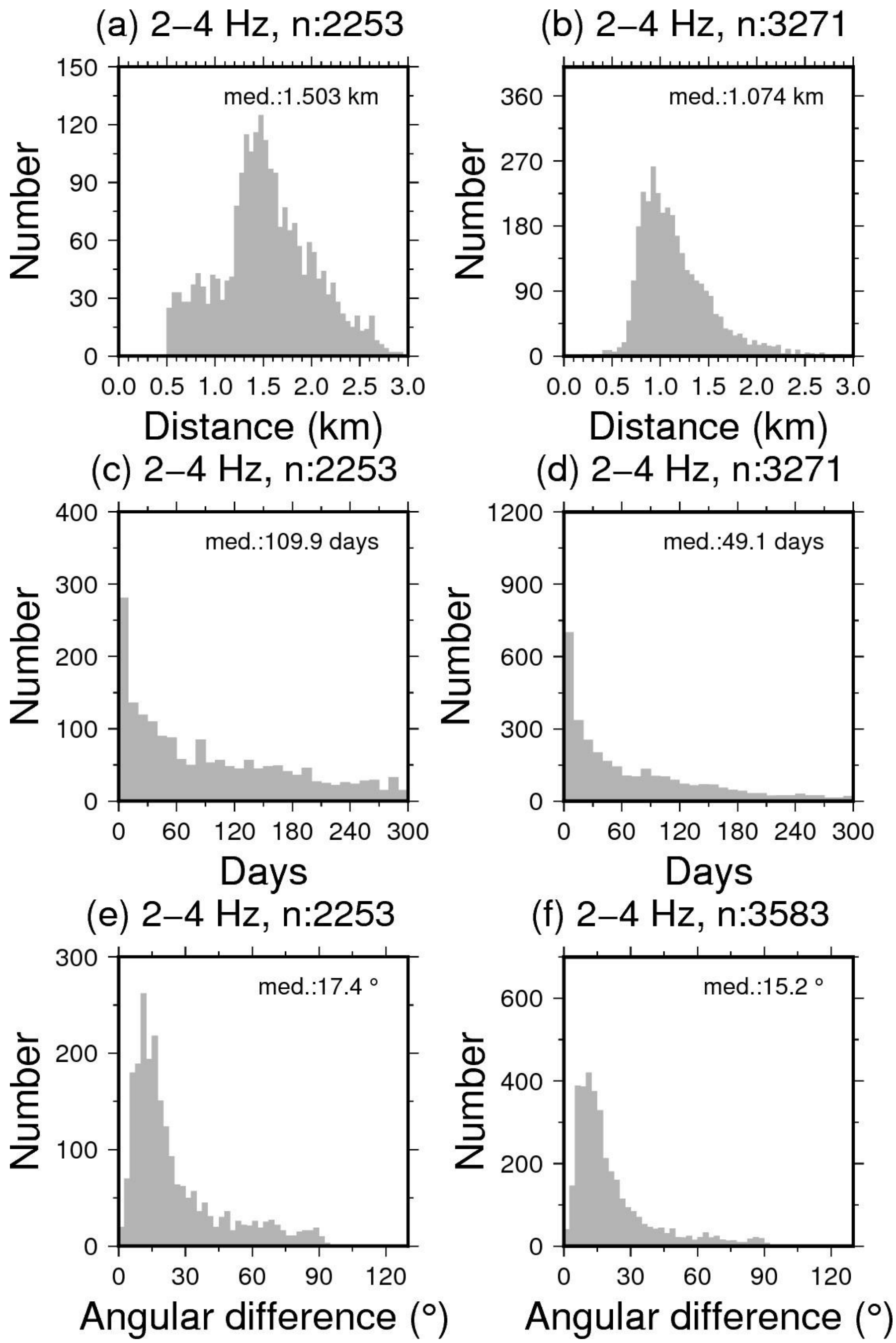

Figure 4. Frequency distributions of (a)–(b) distances, (c)–(d) time intervals, and (e)–(g) 3D angular differences of focal mechanisms for earthquake pairs used to determine Q^{-1}. (a), (c), (e) P-wave; and (b), (d), (f) S-wave.

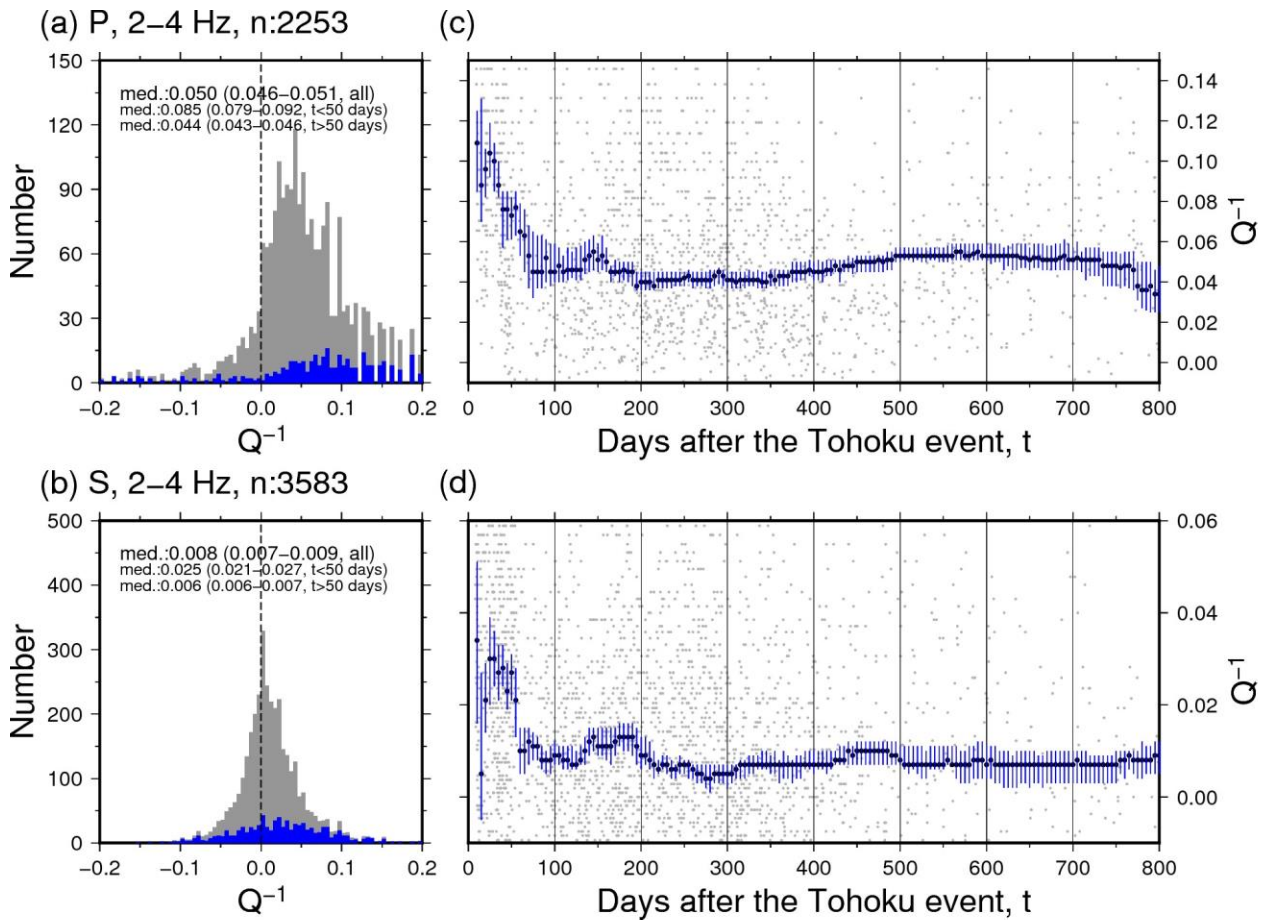

Figure 5. Results of near-source attenuation analyses. (a) Frequency distribution of near-source Q^{-1} values. The grey colour depicts the results for the entire analysed period. The blue colour depicts the results for up to 50 days following the 2011 Tohoku-Oki earthquake; (b) temporal changes in near-source Q^{-1}values. The grey circles show the individual results and the blue circles show the median of each bin. The timing of individual results was set to the mean of the occurrence timing of earthquake pairs. The vertical line indicates the 95 % confidential interval for the median based on 2000 bootstrap re-samplings.

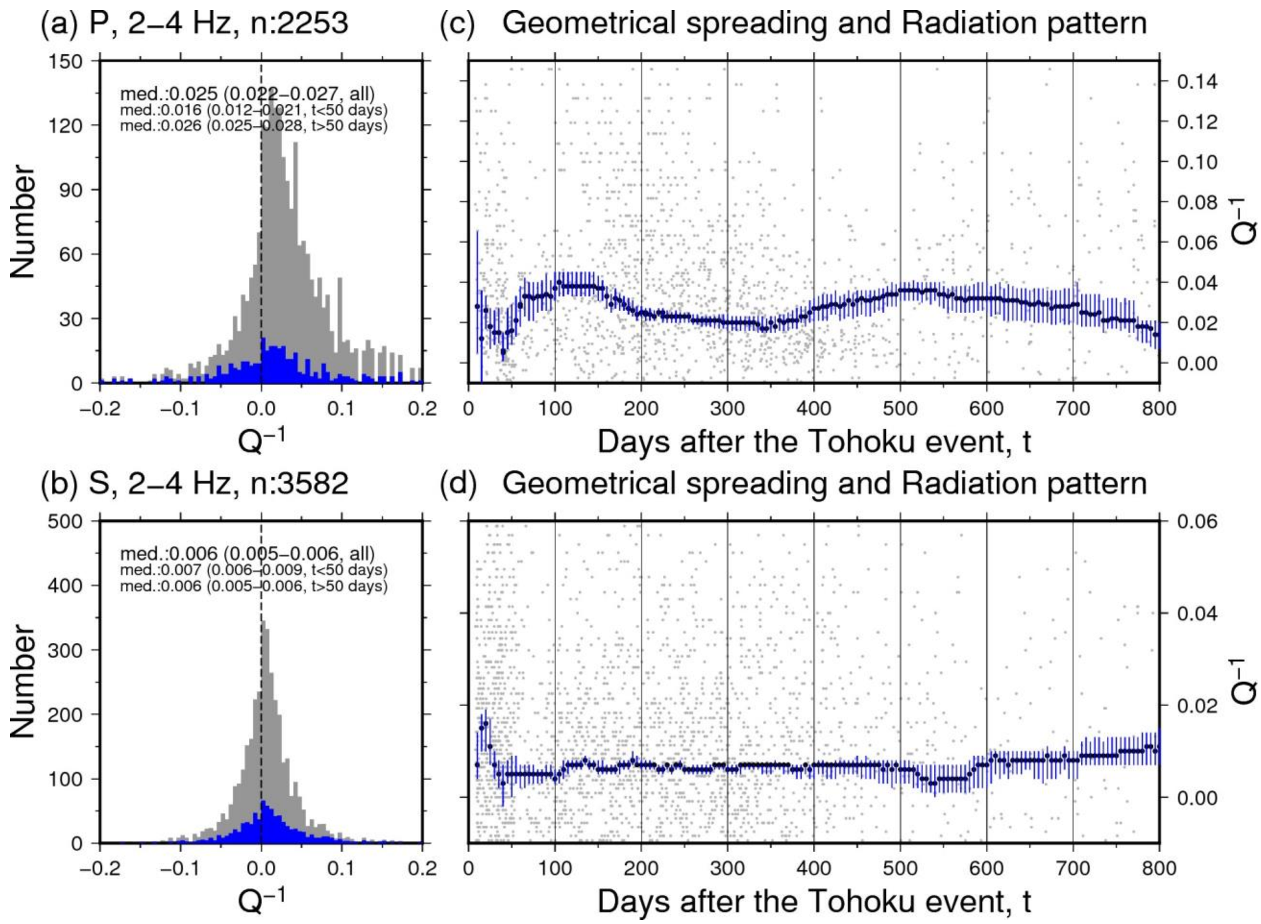

Figure 6. Results of near-source attenuation analyses using synthetic data. Synthetic data was produced by considering the effects of geometrical spreading and radiation pattern. (a) Frequency distribution of near-source Q^{-1}values. The grey colour depicts the results for all analysed periods. The blue colour depicts the results for up to 50 days after the 2011 Tohoku-Oki earthquake; (b) temporal changes in near-source Q^{-1}. The grey circles show individual results and red circles show median values of each time bin. Vertical line indicate the 95 % confidential interval based on 2000 bootstrap re-samplings of individual Q^{-1} values. The other details are the same as per Fig. 4.

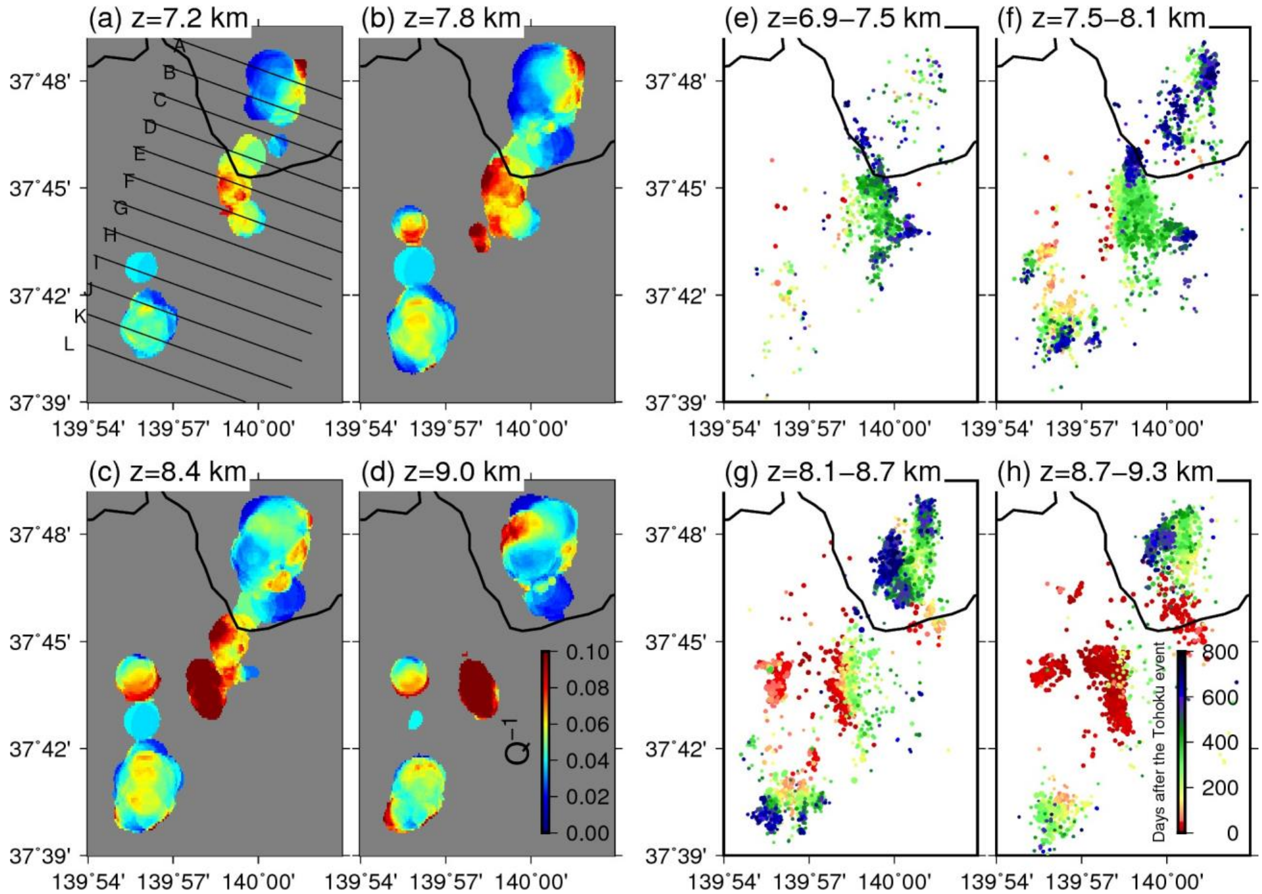

Figure 7. (a)–(d) Spatial distribution of Q^{-1} for the 2–4 Hz frequency range at four different depths. Q^{-1} values are shown by the colour scale; (e)–(f) spatial distribution of hypocentres determined by Yoshida & Hasegawa (2018). Occurrence timings are shown by the colour scale.

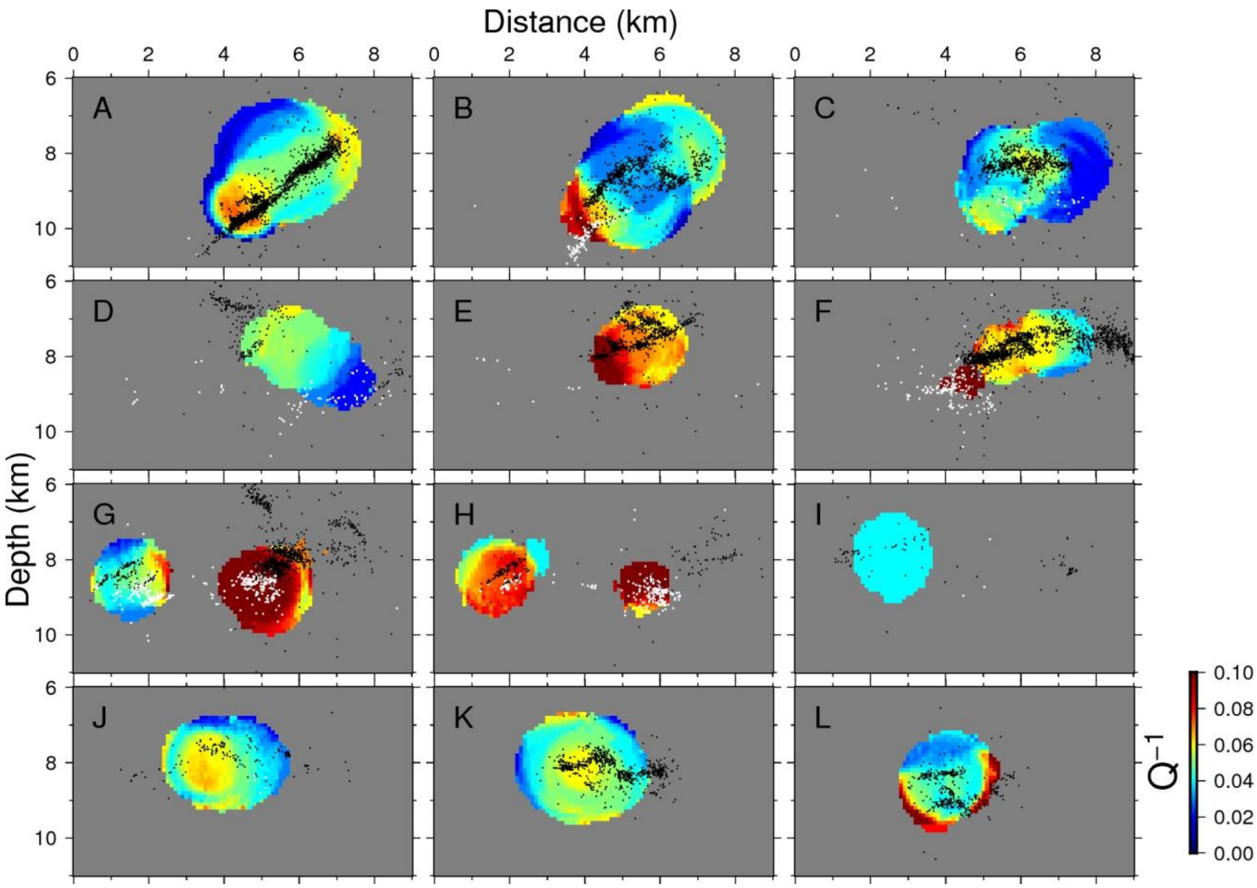

Figure 8. Cross-sectional views of Q^{-1} for the 2–4 Hz frequency range along the lines shown in Fig. 6 (a). Q^{-1} values are shown by the colour scale. White and black circles depict the hypocentres in the initial 50 days and the later period, respectively.

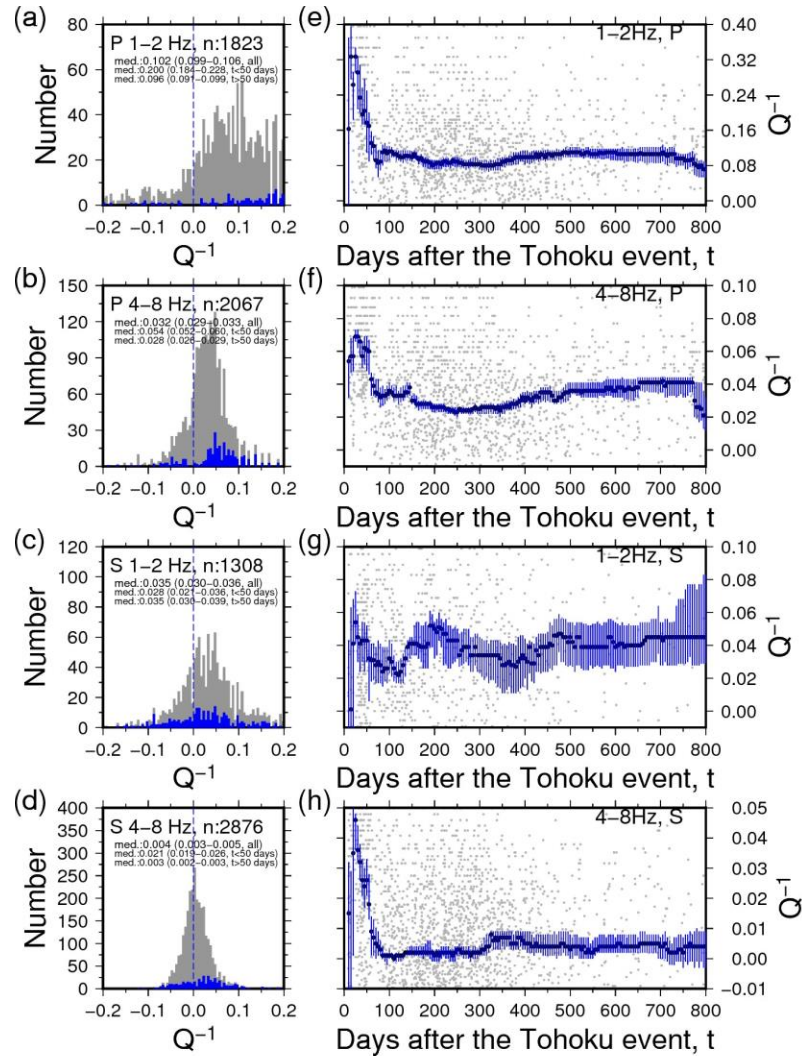

Figure 9. Results of near-source attenuation. (a)–(d) Frequency distribution of near-source Q^{-1}-values; (e)–(h) temporal change in near-source Q^{-1}-values; (a), (e): results for the frequency ranges of 1–2 Hz from P-waves; (b), (f): results for the frequency ranges of 4–8 Hz from P-waves; (c), (g): results for the frequency ranges of 1–2 Hz from P-waves; (d), (h): results for the frequency ranges of 4–8 Hz from P-waves. The grey circles show individual results and red circles show median values of each time bin. The vertical line indicates the 95 % confidence interval based on 2000 bootstrap re-samplings of individual Q^{-1}-values. Other details are the same as per Fig. 4.

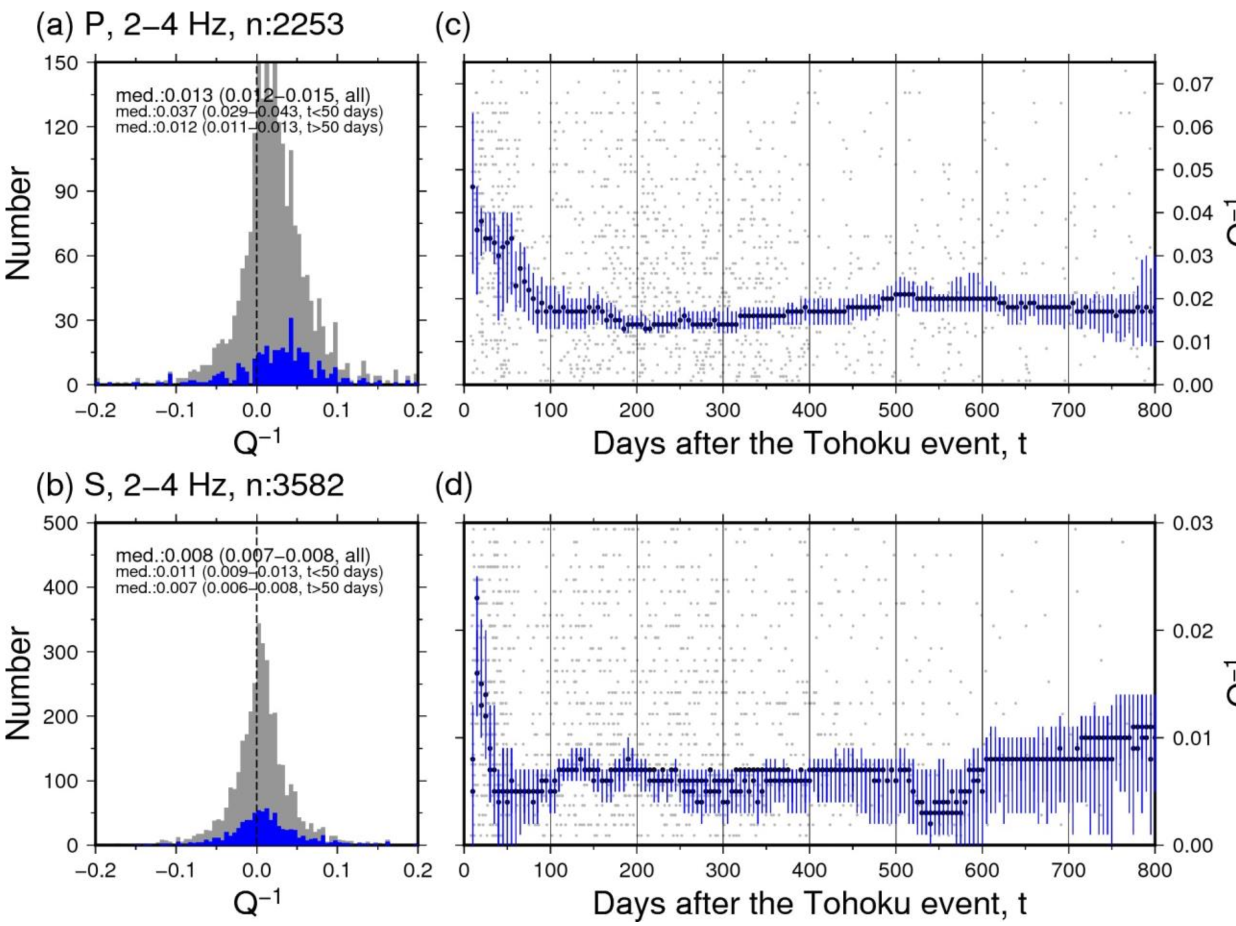

Figure 10. Results of near-source attenuation analyses by accounting for the effects of geometrical spreading and radiation pattern. (a) Frequency distribution of near-source Q^{-1} values. The grey colour depicts the results for all the analysed periods. The blue colour depicts the results for up to 50 days after the 2011 Tohoku-Oki earthquake; (b) temporal changes in near-source Q^{-1} values. The grey circles show individual results and blue circles show median values of each bin. The vertical line indicates the 95 % confidence interval of the median value based on 2000 bootstrap re-samplings. Other details are the same as per Fig. 4.